A comprehensive study on the synchronization procedure in 5G NR with 3GPP-compliant link-level simulator

Riccardo Tuninato[1,4*] , Daniel Gaetano Riviello[2,4] , Roberto Garello[1,4] , Bruno Melis[3] and Roberto Fantini[3]

*Correspondence:
riccardo.tuninato@polito.it

[1] Department of Electronics
and Telecommunications (DET),
Politecnico di Torino, 10129 Turin,
Italy
[2] Department of Electrical,
Electronic, and Information
Engineering (DEI), Università di
Bologna, 40136 Bologna, Italy
[3] TIM S.p.A., 10148 Torino, Italy
[4] Consorzio Nazionale
Interuniversitario per le
Telecomunicazioni (CNIT),
43124 Parma, Italy

Abstract

The 5G New Radio synchronization procedure is the first step that the user must complete to access the mobile network. It mainly consists of the detection of the primary and secondary synchronization signals (PSS and SSS, respectively) and the decoding of the physical broadcast channel (PBCH). Our goal is to provide a comprehensive study of the synchronization procedure and investigate different techniques and approaches, through the implementation of a 5G New Radio-compliant simulator. Of significant interest is the investigation of impairments such as the fading channel, the frequency offset, and the delay spread. The results are provided in terms of detection probability for the PSS and SSS detection, and in terms of block error rate for the PBCH. From the data collected, there is evidence that choosing M-sequences for the PSS leads to an appreciably robust solution against frequency offset. The structure of the Gold sequences for SSS generation can be exploited to reduce the detection complexity, and different approaches can be chosen to improve reliability against delay spread. Moreover, the polar coding for 5G PBCH outperforms the former 4G coding technique, but they are still sensible to frequency offset. Finally, the simulator functionalities are validated through real captures of 5G signals.

Keywords: 5G NR, Synchronization procedure, Initial access, Cell search, SSB, Frequency offset, Signal detection

1 Introduction

The 5th generation (5G) New Radio (NR) mobile communications standard has renewed the physical layer of the previous 4th generation (4G) long-term evolution (LTE) standard. This was necessary to comply with the new requirements defined for 5G, characterized by a wider variety of scenarios and the demands of better performance, not only for what concerns data rates but also for latency and reliability.

One major component of 5G NR is the initial access, the initial step the user equipment (UE) has to carry out to log into the network. In this paper, we investigate the synchronization procedure, the first part of the initial access. During this procedure, the UE has to detect and gain information on the surrounding 5G base stations (BS), i.e. realize a cell search, before trying to perform the random access, which is the second part

Tuninato *et al. J Wireless Com Network* (2023) 2023:111

Page 2 of 29

of the initial access (out of the scopes of this work). An effective synchronization can significantly decrease the communication latency, and the mobile devices must be able to perform the cell search in low signal-to-interference-plus-noise ratio (SINR) conditions, taking care of other impairments, which could disrupt the process. A crucial issue is the alignment of the time–frequency resource grid at the receiver side, which can be achieved by special signals broadcast by the base stations.

5G NR has introduced a key element, the synchronization signal block (SSB). It is a new structure that contains both the primary and secondary synchronization signals (PSS and SSS) and also the physical broadcast channel (PBCH), with its associated demodulation reference signal (DMRS). The entire synchronization procedure is based on the SSB, and its specifications target is one of the key aspects of 5G, flexibility. In fact, it allows more degrees of freedom to the transmitting BS, as an adjustable periodicity of transmission, and the possibility of transmitting the synchronization signals in a set of sparse predefined frequency positions (frequency raster) rather than on the centre of the bandwidth.

Different works addressed the analysis of synchronization signals adopted in 5G NR and presented some implementations and simulations of the techniques to process them, these works are summarized in Table 1. In [1, 2], different correlation-based techniques have been studied for PSS detection, paying attention to the carrier frequency offset (CFO), and similar techniques can be found in [3]. In [4], another version of the PSS detector is based on a prior cyclic prefix (CP) autocorrelation, and, recently, authors in [5] adopted a convolutional neural network solution to address the problem. Studies on SSS and its detection for 5G NR were treated in [6], where a particular transform exploits the M-sequences structure, and a study in [7] provided a different solution in order to keep low the complexity, splitting the SSS detection into two steps. Some analysis on SSS were already available for LTE, as in [8], where the authors compared the use of coherent against non-coherent correlation. For what concerns PBCH, [9] provided a detailed description of the polar encoding and decoding in 5G NR. Even though these studies offer useful results on specific aspects of this topic, there remains a need for the design and evaluation of the entire chain of synchronization functional blocks, starting from the PSS detection in the time domain, before orthogonal frequency-division multiplexing (OFDM) modulation, and down to the PBCH decoding in the frequency domain, after OFDM modulation. The channel constitutes a crucial aspect in a communication system, and, among the most significant channel elements, we find the frequency offset, which can cause a variable phase offset in the time domain (after OFDM modulation) and a much more harmful intercarrier interference (ICI) in the frequency domain (after OFDM demodulation) [10]. It can be mainly caused by the misalignment between the transmitter and receiver local oscillators, or by the Doppler shift, caused by devices moving at relatively high speeds. In [11], authors exploit the PSS and SSS structure to estimate the residual frequency offset (RFO) generated by Doppler shift and estimation errors. Nevertheless, in case of severe Doppler shifts, OFDM modulation is hugely inconvenient [12], because compensation for ICI is a very difficult task. As for the evolution of the standard, many studies have focused on orthogonal time–frequency space (OTFS) modulation, which aims at optimizing the modulation scheme for high Doppler and high delay spread scenarios [13]. Moreover, the authors in [14] highlighted the

good performance of OTFS even in static multipath channels, making it a very promising modulation for future communication systems. However, OFDM modulation is still the most adopted scheme at the moment, and these impairments challenge the 5G NR initial access. Moreover, synchronization will be crucial also for the future coexistence of the terrestrial network with non-terrestrial networks, formed with satellite constellations [15, 16], and when new technologies will be developed, such as the new reconfigurable intelligent surfaces (RIS) [17, 18], which can be used, for example to improve the coverage of the networks, by tuning the reflection angular direction of these particular devices.

Contribution We propose a study of the synchronization procedure with a broader vision, also considering implementation aspects. Our paper takes into account a number of different scenarios, and the developed solutions are also tested with samples from real captured 5G signals. Of particular interest is the impact of impairments such as the wireless channel, the frequency offset, and the Doppler spread. After some analysis with the additive white Gaussian noise (AWGN) channel as a baseline, the simulations are carried out with a more realistic fading channel, which is compliant with the latest 3GPP 3D channel model [19, 20]. Different techniques are compared, and their robustness is assessed against such conditions, in order to provide useful insights for the implementation of the synchronization chain. Moreover, a multiple-input multiple-output (MIMO) system is also considered, which can be used for beam sweeping purposes during initial access. The system is based on the 5G link-level simulator developed by the authors, which already provided the encoding and decoding of the PBCH, but neglected the previous steps, consisting mainly of PSS and SSS detection. The contributions can be summarized as follows:

- Detailed description of the SSB structure and properties for 5G NR synchronization.
- PSS detection analysis in the presence of CFO and fading channel. Implementation aspects are described as the downsampling and the M-sequence properties in 5G-like OFDM systems.
- SSS detection analysis in the presence of CFO and fading channel. Different detection techniques are compared, based on performance and complexity. Moreover, various coherent and non-coherent approaches are tested, previously presented only for LTE, in order to cope with non-idealities such as delay spread (DS).

Table 1 Overview on related works for 5G NR synchronization

Ref	Detection technique
[1]	PSS autocorrelation and cross-correlation with CFO compensation before or after correlation. Results provided for a wide range of carrier frequencies
[2]	PSS cross-correlation for coarse synchronization and triple autocorrelation for fine synchronization
[3]	PSS Coarse synchronization with cross-correlation and fine synchronization with PSS conjugate symmetry-based algorithm
[4]	PSS cross-correlation and autocorrelation with CP. Beam management considerations
[5]	PSS detection with convolutional neural network
[6]	SSS design and detection with the Walsh–Hadamard transform
[7]	Sequential SSS detection by decoupling the detection of two M-sequences for reduced complexity
[8]	Study of SSS detection with both coherent and non-coherent approaches (in 4G LTE)

- Evaluation of the PBCH decoding after PSS, SSS, and DMRS detection, with a focus on CFO impact and comparison with LTE. A simulator for the entire synchronization procedure is thus obtained, providing also MIMO configurations.
- Usage of 5G NR real captures for simulator validation.

Organization This paper is organized as follows: Sect. 2 presents a detailed description of the SSB. In Sect. 3, the system and channel model are described, together with the techniques used at the receiver side for the synchronization procedure. In Sect. 4, the simulation results in different conditions are reported and discussed. Finally, the conclusions are outlined in Sect. 5.

Notation Lower-case and upper-case letters a and A denote the signal vector in the time domain and in the frequency domain, respectively; c^* denotes the conjugate of a complex value c; upper-case boldface letters $\mathbf{A}$ denote a matrix; and $\mathbf{A}^T$ denotes the transpose of matrix $\mathbf{A}$. mod is the modulo operation.

2 Structure of synchronization signal block (SSB)

The synchronization signal block assembles LTE PSS/SSS/PBCH into a single structure, periodically transmitted on the downlink by each NR cell to perform the synchronization procedure [21]. It occupies a total amount of 960 resource elements in the OFDM grid: four OFDM symbols in the time domain and 240 contiguous subcarriers (20 resource blocks) in the frequency domain, for each symbol. Table 2 describes the subcarrier allocation, and Fig. 1a depicts the SSB structure. The actual band in Hz and time duration in sec of the SS block depends on the numerology adopted by the network, and the position in the frequency axis is selected by the BS from a frequency raster, differently from LTE, in which such position is set as the centre of the carrier.

Table 2 Resources within an SS/PBCH block for PSS, SSS, PBCH, and DMRS for PBCH [22]

Channel or signal	OFDM symb numb	Subcarrier number k relative to the start of an SS/PBCH block
PSS	0	$56, 57, \ldots, 182$
SSS	2	$56, 57, \ldots, 182$
Set to 0	0	$0, 1, \ldots, 55$
		$183, 184, \ldots, 239$
	2	$48, 49, \ldots, 55$
		$183, 184, \ldots, 191$
PBCH	1, 3	$0, 1, \ldots, 239\,^*$
	2	$0, 1, \ldots, 47\,^*$
		$193, \ldots, 239\,^*$
DMRS **	1, 3	$0 + v, 4 + v, 8 + v, \ldots, 236 + v$
	2	$0 + v, 4 + v, 8 + v, \ldots, 44 + v$
		$192 + v, 4 + v, 8 + v, \ldots, 236 + v$

* Except for DMRS positions

** $v = N_{\text{ID}}^{cell} \mod 4$

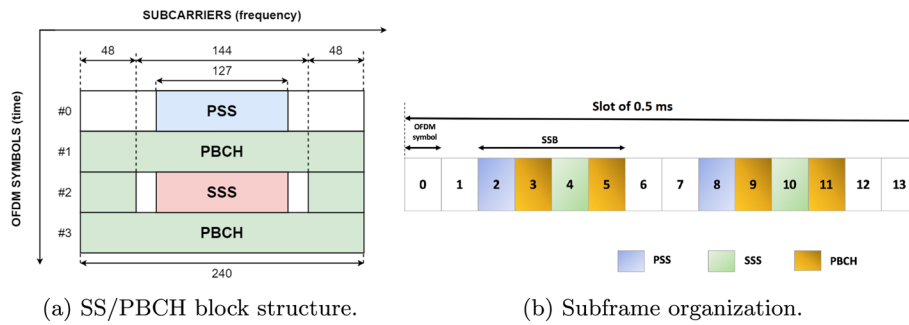(a) SS/PBCH block structure.   (b) Subframe organization.

Fig. 1 SSB properties

2.1 Primary synchronization signal (PSS)

The primary and secondary synchronization signals permit the determination of the physical cell identity (PCID) (or N_{ID}^{cell}) of the cell. In the NR radio interface, the PCID can assume 1008 different values, and it is given by the combination of the cell identity group index $N_{\mathrm{ID}}^{(1)}$ ($\in \{0, 1, \dots, 335\}$) and the physical layer identity within the cell identity group $N_{\mathrm{ID}}^{(2)}$ ($\in \{0, 1, 2\}$). The relation is [22]:

$$N_{\mathrm{ID}}^{cell} = 3N_{\mathrm{ID}}^{(1)} + N_{\mathrm{ID}}^{(2)}. \tag{1}$$

The purpose of PSS is the initial symbol alignment and a coarse frequency correction, since the UE oscillator is characterized by an inaccuracy that could produce a mismatch with the system reference carrier frequency. NR PSS is a FDM-based binary phase shift keying (BPSK) M-sequence of 127 elements, thus occupying 127 subcarriers, out of the 240 of the SS block band. Differently from the SSS, all the remaining SSB subcarriers in the same OFDM symbol are reserved as guard bands, i.e. they are set to zero. There are three different possible sequences p_0, p_1, and p_2, depending on the three different values that $N_{\mathrm{ID}}^{(2)}$ can assume. The sequence $\mathrm{D}_{\mathrm{PSS}}^{(l)}(n)(l = N_{\mathrm{ID}}^{(2)})$ for the PSS is defined by [22]:

$$\mathrm{D}_{\mathrm{PSS}}^{(l)}(n) = 1 - 2\mathrm{P}(m) \qquad m = ((n + 43N_{\mathrm{ID}}^{(2)}) \bmod 127) \qquad 0 \le n < 127 \tag{2}$$

where polynomial $\mathrm{P}(i)$ is given by the recursive formula

$$\mathrm{P}(i + 7) = ((\mathrm{P}(i + 4) + \mathrm{P}(i)) \bmod 2), \tag{3}$$

and it can be computed from its initial values, specified as

$$[\mathrm{P}(6)\ \mathrm{P}(5)\ \mathrm{P}(4)\ \mathrm{P}(3)\ \mathrm{P}(2)\ \mathrm{P}(1)\ \mathrm{P}(0)] = [1\ 1\ 1\ 0\ 1\ 1\ 0].$$

Thus, the three sequences are simply obtained by cyclic shifting one M-sequence. Also in LTE, there were three possible PSSs, but generated as Zadoff–Chu sequences with a length of 62 symbols. The switch to M-sequences is motivated by the time and frequency offset ambiguity affecting Zadoff–Chu sequences: the correlation function outputs undesired periodical peaks along the frequency axis and side peaks along the time axis [23]. 5G then allows the estimation of the frequency offset in one shot, while in LTE, the PSS detection would provide a set of candidates, equispaced in frequency. Moreover, doubling the sequence length results in a 3 dB larger processing gain, but requires longer filters at the receiver side, thus increasing the complexity.

2.2 Secondary synchronization signal (SSS)

Secondary synchronization signal definition is based on cell group id $N_{\mathrm{ID}}^{(1)}$. The design choice for the SSS is a Gold sequence with a chip length of 127, obtained by the combination of two M-sequences. The motivation is that M-sequences are not characterized by good cross-correlation properties, especially if the aim is to form a large set of pseudo-random sequences generated by the same kind of linear-feedback shift register (LFSR) used by the PSS. The sequence $\mathrm{D}_{\mathrm{SSS}}^{(j)}(n)(j = N_{\mathrm{ID}}^{(1)})$ for the secondary synchronization signal is defined by [22]:

$$\mathrm{D}_{\mathrm{SSS}}^{(j)}(n) = [1 - 2S_0((n + m_0) \mod 127)] \cdot [1 - 2S_1((n + m_1) \mod 127)]$$

$$m_0 = 15 \left\lfloor \frac{N_{\mathrm{ID}}^{(1)}}{112} \right\rfloor + 5N_{\mathrm{ID}}^{(2)} \qquad m_1 = N_{\mathrm{ID}}^{(1)} \mod 112 \qquad 0 \le n < 127 \tag{4}$$

where S_0 and S_1 are functions defined as

$$\begin{aligned} S_0(i + 7) &= (S_0(i + 4) + S_0(i)) \mod 2 \\ S_1(i + 7) &= (S_1(i + 1) + S_1(i)) \mod 2 \end{aligned} \tag{5}$$

and S_0 and S_1 assume the same initial values

$$[S_0(6)\ S_0(5)\ S_0(4)\ S_0(3)\ S_0(2)\ S_0(1)\ S_0(0)] = [0\ 0\ 0\ 0\ 0\ 0\ 1]$$
$$[S_1(6)\ S_1(5)\ S_1(4)\ S_1(3)\ S_1(2)\ S_1(1)\ S_1(0)] = [0\ 0\ 0\ 0\ 0\ 0\ 1].$$

These sequences depend on the 1008 values of PCID, but given $N_{\mathrm{ID}}^{(2)}$ recovered from the PSS, the possible SSS candidates reduce to 336. The SSS is located in the 127 central subcarriers of the #2 SSB's OFDM symbol, identified at the receiver side from the PSS position. Since the time and frequency grid should be correctly arranged after PSS detection, the SSS processing by the device can be performed in the frequency domain, after the OFDM Demodulation.

2.3 Physical broadcast channel (PBCH)

The physical broadcast channel is a physical channel used to provide the very first system information [24]:

- System Frame Number (SFN): Similarly to LTE, NR has a 10 bits system frame number starting from 0 to 1023 (for timing purposes);
- Half-frame bit indicator and most significant bits (MSB) of the SS block position within a half-frame (SS block time index);
- Master Information Block (MIB): a minimum amount of system information including how to receive the remaining minimum system information (RMSI). It includes parameters that are needed to acquire system information block 1 (SIB1) from the cell.

The MIB is received by the physical layer after its generation at higher levels, consisting of one transport block of $\bar{A} = 24$ bits (at maximum) every transmission time interval

(TTI) of 80 ms. Before the transmission through the radio channel, it is processed in several steps [22, 25, 26]:

Payload generation The MIB is extended by some timing-related bits: four bits from last significant bits (LSB) of SFN, one bit of half-frame bit, and three additional bits whose value depends on the frequency range. Its length is thus: $A = \bar{A} + 8 = 32$ bits. The payload is then subjected to an interleaving operation [27], to improve the PBCH polar decoder performance and latency.

First scrambling operation PBCH payload is masked (scrambled) with a sequence which shall be initialized with the N_{ID}^{cell} and the 3rd and 2nd LSB bits of SFN (s_2, s_1) carried in the payload. To allow the user to determine the applied mask upon successful polar decoding, in order to reverse scrambling operation, SFN bits, half-frame bit (c_0), and SSB index (b_5, b_4, b_3) remain unmasked. The goal of the scrambling is to obtain randomization of the inter-cell interference by varying the payload along time with SFN bits that change every 20 ms. The 1st scrambling sequence is generated as follows. Let $M(s_2, s_1; N_{\text{ID}}^{cell})$ denotes the M bits long masking sequence with which the PBCH payload is masked before cyclic redundancy code (CRC) attach and polar encoding. Here, M is the number of bits of the PBCH payload that is masked and is equal to $M = A - 3$ for $L_{max} = 4$ or $L_{max} = 8$, and $M = A - 6$ for $L_{max} = 64$ (L_{max} is the maximum number of SS blocks within an SSB burst). With seed $c_{init} = N_{\text{ID}}^{cell}$, generate $4M$ bits long sequence, $C = (c_0, c_1, \ldots, c_{4M-1})$ and cut it in four parts, $C^{(i)} = (c_{Mi}, \ldots, c_{M(i+1)-1})$, for $i \in \{0, 1, 2, 3\}$. Then, select one part based on timing bits (s_2, s_1) as masking sequence, i.e. $M(s_2, s_1; N_{\text{ID}}^{cell}) = C^{(2s_2+s_1)}$.

Transport block CRC attachment A CRC of length $L = 24$ bits is added to the BCH transport blocks in order to detect errors over the transmitted bits. The L CRC parity bits are computed on the entire transport block, using the generator polynomial $G_{CRC24C}(x)$ [25]:

$$G_{24C}(x) = x^{24} + x^{23} + x^{21} + x^{20} + x^{17} + x^{15} + x^{13} + x^{12} + x^8 + x^4 + x^2 + x + 1.$$
(6)

The total length of the sequence becomes $B = A + L = 32 + 24 = 56$ bits.

Channel encoding and rate matching Polar coding is the channel encoding technique adopted for PBCH transmission. It is based on a recursive structure with quite low complexity, based on the principle of "Channel Polarization": Starting from a single channel, it is possible to derive N copies of it, among which some of them are completely noiseless while others completely noisy [9, 28]. Decoding relies on successive cancellation and list decoding. At the output of the encoder, the sequence generated is $N = 2^9 = 512$ bits long. A rate matching block then applies bit repetition to obtain a sequence of length $E = 864$ bits, with $E > N$.

Second scrambling operation After encoding, an additional scrambling is applied, based on N_{ID}^{cell}. The 2nd scrambling sequence is generated as follows. For $L_{max} = 4$ (i.e. below 3 GHz), let $C(b_1, b_0; N_{\text{ID}}^{cell})$ denotes the E bits long masking sequence, the PBCH coded bits are masked after rate matching. The bits b_1, b_0 are the two least significant bits of the SSB index. With seed $c_{init} = N_{\text{ID}}^{cell}$, generate a $4E$ bits long sequence, $C = (c_0, c_1, \ldots, c_{4E-1})$ and cut it in four parts, $C^{(i)} = (c_{Ei}, \ldots, c_{E(i+1)-1})$, for $i \in \{0, 1, 2, 3\}$. Then, select a part based on SSB index bits (b_1, b_0) as masking sequence, i.e. $M(b_1, b_0; N_{\text{ID}}^{cell}) = C^{(2b_1+b_0)}$.

For $L_{max} = 8$ and $L_{max} = 64$ (i.e. above 3 GHz), the same method is applied with the unique difference that the three least significant bits of the SSB index are used. In this case, with seed $c_{init} = N_{\mathrm{ID}}^{cell}$, generate $8E$ bits long sequence, $\mathrm{C} = (c_0, c_1, \ldots, c_{8E-1})$ and cut it in eight parts, $\mathrm{C}^{(i)} = (c_{Ei}, \ldots, c_{E(i+1)-1})$, for $i \in \{0 \ldots 7\}$. Finally, select one part based on SSB index bits (b_2, b_1, b_0) as masking sequence, i.e. $\mathrm{M}(b_2, b_1, b_0; N_{\mathrm{ID}}^{cell}) = \mathrm{C}^{(4b_2 + 2b_1 + b_0)}$.

Modulation and mapping to resources The PBCH symbols are quadrature phase shift keying (QPSK) modulated, resulting in a block of complex-valued symbols. The last PBCH-specific processing is the mapping of the modulation symbols into the time and frequency physical resources, i.e. the resource blocks (RB) within the SSB (Table 2).

2.4 Demodulation reference signals (DMRS) for PBCH

DMRS is introduced to permit the coherent demodulation of PBCH at the UE, since it is designed for radio channel estimation. In Sect. 7.4.1.4 of [22], the definition of the reference signal sequence is reported. The DMRS is associated to the PBCH, and they are mapped jointly in the RB grid (Table 2). The DMRS shift in the frequency position is determined by v, given by $v = N_{\mathrm{ID}}^{cell} \bmod 4$. Thus, this value depends on the cell ID, which can be derived in advance by PSS and SSS detection. The DMRS sequence is localized by the receiver within the SSB, enabling the successive PBCH recovery. The actual transmitted sequence can be found through the cross-correlation function with a list of local replicas of DMRS sequences that can be realized in either a coherent or non-coherent way [29]. The coherent detection is implemented whether the received sequence has been firstly compensated for phase and amplitude variations introduced by the channel (for example using SSS as a phase reference). It assures better performance than the non-coherent case but at the price of increased complexity. The detection of the correct sequence provides the LSB part of the SSB index, thus each SSB detection can be made independently from the others.

3 Methodology

3.1 System model

In 5G NR systems, the OFDM modulation involves the signal description in both the frequency and time domains. Assuming an OFDM modulation with N_{FFT} points for the fast Fourier transform (FFT) and inverse FFT (IFFT), let us denote the transmitted signal in the time domain $\mathrm{x}(n)$ as [30]

$$\mathrm{x}(n) = \sum_{m=0}^{N_{\mathrm{FFT}}} \mathrm{X}(m) e^{j2\pi mn/N_{\mathrm{FFT}}} \tag{7}$$

with $m, n \in \{0, \ldots, N_{\mathrm{FFT}}\}$ and $\mathrm{X}(m)$ the transmitted signal in the frequency domain, composed by M-PSK or M-quadrature amplitude modulation (QAM) symbols, each assigned to a different subcarrier. In the case of AWGN channel, the received signal in the frequency domain $\mathrm{Y}(m)$ is given by:

$$Y(m) = \sum_{n=0}^{N_{\text{FFT}}} y(n)e^{-j2\pi mn/N_{\text{FFT}}} = \sum_{n=0}^{N_{\text{FFT}}} (x(n) + w(n))e^{-j2\pi mn/N_{\text{FFT}}}$$
$$= X(m) + W(m)$$

(8)

with $y(n)$ the received signal in the time domain, $w(m)$ the complex additive white Gaussian noise with zero mean and variance N_0, and $W(m)$ the FFT of $w(n)$. The problem becomes more tricky when considering a frequency offset Δf, resulting in a multiplicative factor in the time domain $e^{j2\pi n\Delta f/f_s}$, with f_s the sampling frequency. Thus, the frequency offset produces a time-variable phase shift in the time domain, which translates into ICI in the frequency domain, as described in [10].

3.2 Channel model

In order to collect valuable results from our system, a fading channel is considered. Its generation is based on the 3D stochastic channel for 5G mmWave massive MIMO communications released by 3GPP in TR 38.901 [19]. It is a 3D model because waves are considered to propagate along both horizontal and vertical planes, and so the elevation of the devices is taken into account, a crucial aspect in mmWave communications. In fact, the channel model is designed for the frequency range from 0.5 to 100 GHz, and it is based on a clustered delay line (CDL) model: The propagation path is shaped as a set of clusters distributed over the area, which group the scatterers and so different replicas of the propagated signal (i.e. different rays). A certain number of clusters are generated at each iteration, depending on the scenario (e.g. urban micro or urban macro), and are characterized by a set of angular directions relative to their position in the space, as the azimuth of arrival and departure, and zenith of arrival and departure. Furthermore, each cluster additionally produces a different delay and power gain and contains a set of rays. A ray is characterized by certain angular directions, generated from the angular directions of its cluster. Further details on the adopted channel model and its implementation can be found in [20, 31, 32]. The coherence time of the channel depends on the Doppler spread, and so on the user speed, which is fixed at 3 km/h (i.e. a walking pedestrian). The coherence bandwidth instead depends on the delay spread, which can be selected among the set {"VERY SHORT", "SHORT", "NOMINAL", "LONG", and "VERY LONG"}. In our simulator, the CDL-B profile is adopted, specifically for non-line-of-sight (NLOS) transmissions. The user is placed at a distance of 100 m from the BS, with a height of 1.5 m, while the BS has a height of 10 m.

The received signal in case of the fading channel can be written as follows:

$$Y(m) = H(m)X(m) + W(m)$$

(9)

with $H(m)$ the FFT of $h(n)$, the time-domain channel response.

3.3 PSS detection

The signal reaching the receiver must be processed in the time domain before the FFT can be applied, because prior to synchronization, the receiver is not aligned either in time or frequency. Firstly, the signal goes through the receiver's front end, and the signal must be filtered for the frequency range outside the frequency band. Moreover, the frequencies outside the SSB boundaries should be removed. In this way, the

receiver deals with a limited portion of the signal bandwidth to facilitate synchronization. The resulting signal is downsampled to get a bandwidth B_s of:

$$B_s = \Delta f_{SCS} \cdot N_{subcarriers} = 30\text{kHz} \cdot 256 = 7.68\text{MHz} \tag{10}$$

where Δf_{SCS} is the subcarrier spacing (SCS) (chosen equal to 30 kHz as in Table 5), and $N_{subcarriers}$ is chosen as the first power of 2 largest than the number of subcarriers occupied by the SSB, which are 240. This step is crucial because the detectors in the time domain are implemented as matched filters, and their length cannot be the same as the number of subcarriers adopted by the system; otherwise, the complexity would be too high. Even if the system adopts an FFT of larger dimension ($N_{FFT}^{sys} = 4096$), the detectors can be realized through matched filters of 256 taps long. Accordingly, we adopt $N_{FFT} = 256$ per OFDM symbol for the SSB processing. In order to filter out the frequencies outside the SSB but also prevent degradation of the synchronization procedure, we deploy a suitable anti-aliasing low pass filter, with Kaiser–Bessel window [33]. For the actual PSS detection technique, three different approaches have been studied in [1], one exploiting autocorrelation and two cross-correlation. Their results depend on parameters such as SINR, carrier frequency (f_c), and carrier frequency offset (CFO or Δf_c). After analysing those results, and looking at results for a f_c close to our case, the more robust one appears to be *cross-correlation-based PSS detection before FO estimation and compensation* [1]. The cross-correlation of the received signal and a local replica of the PSS sequences results in a correlation value for each time delay and for each of the three PSS sequence candidates. The parameter timing $\hat{\mu}_t$ and the actual PSS sequence $\hat{l}$ (one out of three) can then be determined by looking at the arguments giving the maximum correlation value:

$$\left(\hat{\mu}_t, \hat{l} \right) = \arg\max_{\mu_t, l} \left| \sum_{n=0}^{N_{FFT}-1} y(n + \mu_t) \cdot \hat{d}_{PSS}^{(l)}(n)^* \right|^2. \tag{11}$$

The maximum is then found with an exhaustive search over the results of the correlation metric. Figure 2 shows the entire block scheme of the PSS detector. In LTE, an alternative solution is the detection of the CP via autocorrelation, to align the receiver in the time grid, and then, detection of the PSS is done after OFDM demodulation in the frequency domain. This could be more challenging in 5G NR, due to the signal chosen for the PSS. The explanation follows.
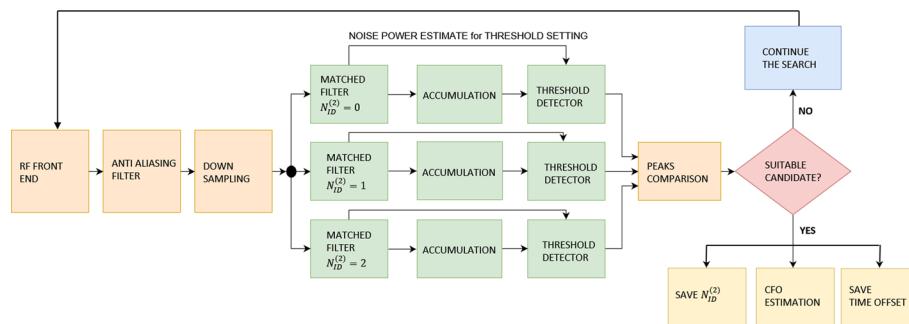

Fig. 2 Block scheme for the PSS detector

3.3.1 Details on the properties of M-sequences for PSS

The design choice of using M-sequences instead of Zadoff–Chu sequences has been explained in the previous Sect. 2.1. Nevertheless, M-sequences are characterized by very good autocorrelation properties, but not very good cross-correlation properties, since a set of M-sequences generated by the same kind of LFSR are simply delayed versions of the same sequence. This problem is shown in Fig. 3a and b, for 5G PSS linear and circular correlation in the frequency domain (before OFDM modulation), which is more evident in the latter. This is the reason why the detection of PSS after FFT could be not ideal, which instead was a viable solution in LTE. M-sequences are still an efficient solution because OFDM changes the domain of the signal: From the properties of FFT, the correlation in the new domain corresponds to apply the IFFT to bitwise multiplication of the transformed sequences. In Fig. 4a and b, the behaviour of the PSS correlation is shown in the time domain (after OFDM demodulation). Moreover, M-sequences are a valuable solution for the simple implementation of the LFSR, which can be reused for the generation of the Gold codes for the SSS.

3.3.2 Frequency offset estimation and compensation

The carrier frequency offset can be expressed as the sum of an integer frequency offset (IFO) term and a fractional frequency offset (FFO) term, whose values depend on the SCS used by the system:

$$FO = FFO + IFO \cdot \Delta f_{SCS}. \tag{12}$$

If the CFO value approaches the SCS or even surpasses it, the detection may fail. This means that the previous correlation operation should be performed also for different values of IFO, possibly in parallel:
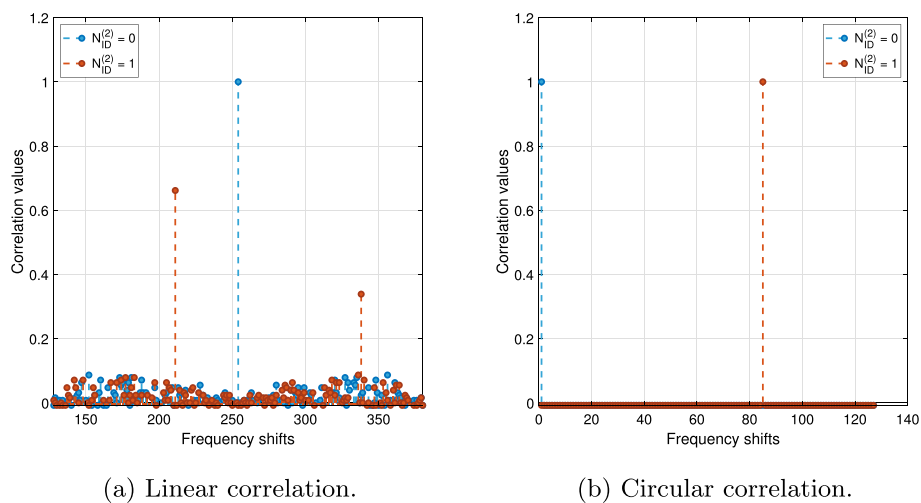

(a) Linear correlation.   (b) Circular correlation.

Fig. 3 PSS M-sequences correlation properties in the frequency domain

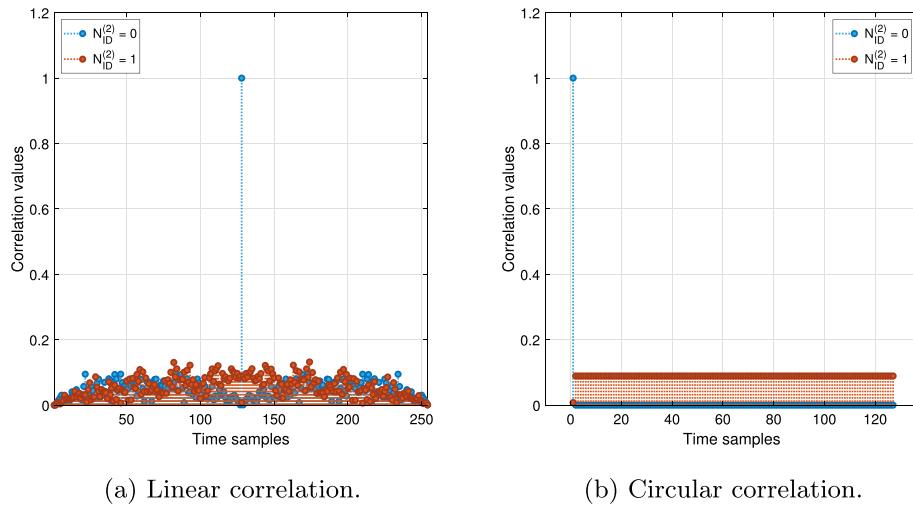(a) Linear correlation.   (b) Circular correlation.

Fig. 4 PSS M-sequences correlation properties in the time domain

Table 3 Values of CFO for different possible oscillators' accuracy

f_c GHz	Non-initial acquisition $\varepsilon = 0.1$ ppm kHz	Initial acquisition $\varepsilon = 5$ ppm kHz
1.8	0.18	9
3.6	1.8	18
6	0.6	30
36	3.6	180
60	6	300

$$\left(\hat{G}, \hat{\mu}_t, \hat{l}\right) = \arg\max_{G, \mu_t, l} \sum_{G=-m}^{m} \left| \sum_{n=0}^{N_{\text{FFT}}-1} \tilde{y}_G(n + \mu_t) \cdot \hat{d}_{\text{PSS}}^{(l)}(n)^* \right|^2 \tag{13}$$

where G is the IFO, and $\tilde{y}_G(n + \mu_t)$ is the received signal compensated for the possible IFO, given by

$$\tilde{y}_G(n + \mu_t) = y(n + \mu_t) \cdot e^{(-j2\pi \Delta f_{\text{SCS}} G / f_s)}. \tag{14}$$

The problem of IFO is crucial in the initial acquisition stage when the user has not performed any correction yet. In this condition, the CFO considered for LTE receivers was 5 ppm, but with 5G NR, more accurate oscillators could be available. When the UE is already connected to a base station, for example in case, it wants to monitor the nearby stations for handovers, the expected CFO value should be in the order of the 0.1 ppm [34], far lower than the SCS. In Table 3, the two possible values of CFO are reported for different f_c. Considering a carrier frequency of 3.6 GHz for our system, the CFO could be up to/down to ± 18 KHz. With an SCS of ± 30 KHz, the detector should try three possible values of IFO: -1, 0, and $+1$. In a real scenario, the user must additionally take into account the different 5G frequency bands, so test the frequency position candidates of the SSB from the frequency raster.

Once the IFO is found, the FFO can be estimated. Through the received timing $\hat{\mu}_t$ and sequence $\hat{l}$ of the PSS, we compute the partial correlation between the received PSS signal and PSS sequence replica over the former and latter $N_{\text{FFT}}/2$ sample duration of the PSS [1] as

$$
\begin{aligned}
C_0 &= \sum_{n=0}^{N_{\text{FFT}}/2-1} \text{y}(n + \hat{\mu}_t) \cdot \hat{\text{d}}_{\text{PSS}}^{(\hat{l})}(n)^* \\
C_1 &= \sum_{n=0}^{N_{\text{FFT}}/2-1} \text{y}(n + N_{\text{FFT}}/2 + \hat{\mu}_t) \cdot \hat{\text{d}}_{\text{PSS}}^{(\hat{l})}(n)^*.
\end{aligned}
\tag{15}
$$

Based on these partial correlations, the phase variation $\Delta\hat{\theta}$ due to the frequency offset over $N_{\text{FFT}}/2$ sample duration is estimated as

$$
\Delta\hat{\theta} = \arg\left(\frac{\text{Im}\{C_1 \cdot C_0^*\}}{\text{Re}\{C_1 \cdot C_0^*\}}\right),
\tag{16}
$$

and finally, the fractional frequency offset is computed from $\Delta\hat{\theta}$:

$$
\Delta\tilde{f} = \frac{\Delta\hat{\theta} \cdot f_s}{\pi N_{\text{FFT}}}.
\tag{17}
$$

Since $\Delta\hat{\theta}$ is periodic, also it is $\Delta\tilde{f}$, allowing us to estimate Δf_c in a range of $\pm\Delta f_{\text{SCS}}$. Differently from [1], we use the arg function to recover $\Delta\hat{\theta}$, instead of $\tan^{-1}$. This choice could avoid the additional step of IFO estimation if the CFO is in the range of $\pm\Delta f_{\text{SCS}}$. However, the PSS detection degrades for CFO outside the range $\pm\Delta f_{\text{SCS}}/2$.

3.4 SSS detection

After the PSS detection, the signal goes through the OFDM demodulator, and the signal in the frequency domain is recovered from the subcarrier positions. The receiver can then perform SSS detection to determine $N_{\text{ID}}^{(1)}$. Many techniques are available, providing optimal or sub-optimal solutions, and different complexities.

3.4.1 Brute force

The simplest detection technique, brute force, consists of computing the cross-correlation Φ_{SSS} of the received samples $\text{Y}(m)$ among all the possible SSS sequences $\text{D}_{\text{SSS}}^{(j)}$, which are 336 out of 1008, as

$$
\Phi_{\text{SSS}}^{(j)} = \sum_{m=0}^{127} \text{R}_{\text{SSS}}(m) \cdot \text{D}_{\text{SSS}}^{(j)}(m)^*
\tag{18}
$$

where R_{SSS} is the portion of the received signal $\text{Y}(m)$ containing the SSS, and $j \in \{0\ldots335\}$ are the potential candidates for $N_{\text{ID}}^{(1)}$. The corresponding estimated group id $\hat{N}_{\text{ID}}^{(1)}$ is then the one maximizing the correlation function:

$$
\hat{N}_{\text{ID}}^{(1)} = \arg\max_{(j)} \left|\Phi_{\text{SSS}}^{(j)}\right|^2.
\tag{19}
$$

Despite the simplicity, and being the optimal solution (for an AWGN channel), its complexity is quite high, since it requires $336 \times (127 - 1)$ additions.

3.4.2 Fast Walsh–Hadamard transform (FWHT)-based detection

This technique takes advantage of the analogy between M-sequences and Walsh–Hadamard codes. In fact, it is possible to demonstrate that the matrix of all possible M-sequences (fixed to a certain length) is just a rows and columns permutation of the Hadamard matrix and vice versa [6]:

$$\hat{\mathbf{M}} = \hat{\mathbf{L}} \cdot \hat{\mathbf{S}} = \mathbf{P}_S \cdot \mathbf{B} \cdot \mathbf{B}^T \cdot \mathbf{P}_L = \mathbf{P}_L \cdot \mathbf{H} \cdot \mathbf{P}_S \tag{20}$$

where:

- $\mathbf{M} = \mathbf{L} \cdot \mathbf{S}$ is the M-sequence matrix of dimension $[2^n - 1 \times 2^n - 1]$, i.e. the matrix whose rows are all the possible cyclic shift of the M-sequence generated by a certain LFSR of length n.
- $\mathbf{S}$ is a $[n \times 2^n - 1]$ matrix formed by the first n rows of $\mathbf{M}$.
- $\mathbf{L}$ is a $[2^n - 1 \times n]$ binary matrix in which the first n rows form an identity matrix of order n. It is found by computing: $\mathbf{L} = \mathbf{S}^T \cdot \Sigma^{-1}$, with Σ a square matrix formed by the first n columns of $\mathbf{S}$.
- $\hat{\mathbf{S}}$ is $\mathbf{S}$ bordered by a first column of all zeros, and $\hat{\mathbf{L}}$ is $\mathbf{L}$ bordered by a first row of all zeros.
- $\hat{\mathbf{M}} = \hat{\mathbf{L}} \cdot \hat{\mathbf{S}}$ is the bordered $\mathbf{M}$ matrix of dimension $[2^n \times 2^n]$
- $\mathbf{B}$ is the $[2^n \times n]$ matrix which rows are the first 2^n ordered numbers in binary representation.
- $\mathbf{H} = \mathbf{B} \cdot \mathbf{B}^T$ is the Hadamard matrix of dimension $[2^n \times 2^n]$.
- $\mathbf{P}_S$ and $\mathbf{P}_L$ are the permutation matrices of dimension $[2^n \times 2^n]$ such that $\hat{\mathbf{L}} = \mathbf{P}_L \cdot \mathbf{B}$ and $\hat{\mathbf{S}} = \mathbf{B}^T \cdot \mathbf{P}_S$

The correlation values are then computed via the FWHT, taking advantage of the low complexity of this operation. Actually, the FWHT operation can be called M-sequence transform, described in detail in [35]. It is accomplished by:

1. Reordering the received sequence according to a permutation matrix $\mathbf{P}_S$.
2. Performing the fast Walsh–Hadamard transform (FWHT).
3. Reordering the transformed data according to a permutation matrix $\mathbf{P}_L$.

The overall detection algorithm is then described:

1. UE tries to remove the effect of the BPSK modulated $S_{0,a}$, the first of the two M-sequences, from the received signal by element-wisely multiplying them. The first possible value of m_0 is chosen as the a hypothesis.
2. Assuming that the hypothesis on the cyclic shift of $S_{0,a}$, m_0, is correct, the obtained new sequence $\hat{R}_{SSS}$ should only contain the second BPSK modulated sequence S_{1,m_1} (plus noise or interference terms), related to the unknown cyclic shift m_1. At

this point, the FWHT operation can be performed to compute the inner products between $\hat{R}_{SSS}$ and all the 112 cyclically shifted versions of S_{1,m_1} in an efficient way.

3. If the hypothesis on m_0 is correct and the FWHT operations output a sufficiently high peak, we choose the corresponding $\hat{m}_0$ and $\hat{m}_1$ as the estimated cyclic shifts, to recover $N_{ID}^{(1)}$.

4. Since a can assume three different values (from the definition of m_0), this operation is repeated for other two distinct iterations (three in total). If different peaks are found in different iterations, the highest one is kept. If in any iteration no peaks are found, SSS is not detected.

The author of [6] states that this technique keeps the complexity very low, since the FWTH operation implies a complexity of $N \log(N)$, which is iterated for each possible hypothesis of m_0. Since they are 3, this technique involves $3 \times 127 \times \log_2(127 + 1)$ additions. In [6], the performance reported shows great improvement with respect to the LTE SSS detection, but there is no comparison between this technique and the standard one.

We show here that this technique assures virtually the same performance, from a probability of missed detection point of view, as the brute detection:

- Looking at the brute force technique, one could separate the correlation into two steps, multiplying the incoming bits with the first M-sequence and then correlating with the second one, and the same result would be obtained:

$$
\begin{aligned}
\Phi_{SSS}^{(j)} &= \sum_{m=0}^{127} R_{SSS}(m) \cdot D_{SSS}^{(j)}(m)^* = \sum_{m=0}^{127} R_{SSS}(m) \cdot \left(S^{(a)}(m) \cdot S^{(b)}(m) \right)^* \\
&= \sum_{m=0}^{127} \left(R_{SSS}(m) \cdot S^{(a)}(m)^* \right) \cdot S^{(b)}(m)^* = \sum_{m=0}^{127} \hat{R}_{SSS}(m) \cdot S^{(b)}(m)^*.
\end{aligned}
\tag{21}
$$

  Thus, removing the first of the two M-sequences in the FWHT-based technique does not change the result.

- Computing the WHT (without the fast implementation) would just be, from a computational point of view, the multiplication and then the sum of the interested samples with all the possible basis functions, equivalently to the correlation operation.

- Furthermore, exploiting the fast version of the WHT does not lead to noticeable errors with respect to the plain transform, and permutations do not imply any alteration in the correlation output, since only the absolute order of the bits composing the sequences is changed: At the end, the same pair of values are multiplied.

3.4.3 Sequential SSS detection

In [7], the authors present a low-complexity detection technique, by taking advantage of good autocorrelation property between cyclic-shifted versions of M-sequence. The search space of SSS hypothesis testing can be reduced by decoupling the detection of two M-sequences. The combination of such a sequential strategy with maximum likelihood detection criterion should facilitate low complexity and reliable SSS detection in the 5G

NR system. This is clearly a sub-optimal solution, increasing the noise harm due to the autocorrelation. The paper indicates a performance drop from standard techniques of approximately more than 3 dB in AWGN channel and flat fading channel, but saving nearly two-thirds of the computational complexity. Anyway, results get even worse when dealing with frequency-selective channels.

3.5 SSS detection solutions against delay spread

The previous techniques were focused on the complexity of the SSS detector. One factor that could decrease the effectiveness of this block is the delay spread, since it leads to a frequency-selective channel, a factor that can degrade the signal quality. In [8], the problem is tackled in LTE by using different approaches to the SSS detection, trying to decrease the effect of different shifts among the subcarriers:

Non-coherent full block detection Same approach as described previously, valid for both the brute force and FWHT techniques.

Non-coherent detection—Differential correlation based Differential correlation is used for coarse frequency synchronization, and it can be used for non-coherent detection of SSS. The correlation output of differential correlation is the complex conjugate product between adjacent descrambled signals [8]:

$$\hat{N}_{\text{ID}}^{(1)} = \arg\max_{(j)} \left| \sum_{m=0}^{127} \text{R}_{\text{SSS}}(m)\text{R}_{\text{SSS}}(m-1)^* \text{D}_{\text{SSS}}^{(j)}(m)\text{D}_{\text{SSS}}^{(j)}(m-1)^* \right|^2. \tag{22}$$

In our system, the differential correlation-based non-coherent detection can be robust against a frequency-selective fading channel, because the term $\text{R}_{\text{SSS}}(m)\text{R}_{\text{SSS}}(m-1)^*$ can reduce channel effect. However, this operation induces SINR loss due to the squaring of the complex conjugate noise product.

Non-coherent partial blocks detection Cross-correlation is applied to the entire sequences of the received signal and reference signal. The integration range of the correlation can instead be divided into a number of small blocks. The output is the sum of the correlation values obtained from the different blocks and can be written as [8]

$$\hat{N}_{\text{ID}}^{(1)} = \arg\max_{(j)} \sum_{b=0}^{M-1} \left| \sum_{m=bN_M}^{(m+1)N_M-1} \text{R}_{\text{SSS}}(m)\text{D}_{\text{SSS}}^{(j)}(m)^* \right|^2 \tag{23}$$

where M is the number of blocks, and N_M is the number of samples in each block. M can be defined as a fundamental design parameter and should be chosen according to the coherence bandwidth of the multipath fading channel, and the authors set it at $M = 3$. This approach cannot be applied with the FWHT technique.

Coherent detection For coherent detection, the UE can estimate the channel frequency response $\tilde{\text{H}}_{\text{PSS}}(m)$ by using the received PSS sequence. The SSS detection is done after the PSS detection, and the channel can, therefore, be assumed to be known based on the PSS sequence, assuming a sufficient coherence time. In the frequency domain, the sequence resulting from SSS and channel compensation is given by [8]

$$\tilde{\text{R}}_{\text{SSS}}(m) = \text{R}_{\text{SSS}}(m)\tilde{\text{H}}_{\text{PSS}}(m)^*. \tag{24}$$

Table 4 Complexity comparison for the proposed techniques

Signal	Objective	Eq.	Complexity (operations)
PSS	$\mu_t, N_{ID}^{(2)}$, IFO	13	IFO candidates $\times 3 \times 2 \times N_{FFT} = 182 \times N_{FFT}$
	FFO	15	$2 \times (N_{FFT}/2) + 2 = N_{FFT} + 2$
SSS	$N_{ID}^{(1)}$	18	$2 \times (336 \times 127) = 85344$
	$N_{ID}^{(1)}$	20	$3 \times 127 \times \log_2(127 + 1) = 2667$
	$N_{ID}^{(1)}$, DS mitigation (non-coh. diff.)	22	$2 \times (336 \times 3 \times 127) = 256032$
	$N_{ID}^{(1)}$, DS mitigation (non-coh. part. blocks)	23	$2 \times (336 \times 127) = 85344$
	$N_{ID}^{(1)}$, DS mitigation	24	$2 \times 127 + 2 \times (336 \times 127) = 85598$
	(coherent)		$2 \times 127 + 2 \times (3 \times 127 \times \log_2(127 + 1)) = 2921$

length PSS = length SSS = 127
$N_{ID}^{(1)}$ candidates = 336
$N_{ID}^{(2)}$ candidates = 3

The correlation is then computed as usual, replacing R_{SSS} with $\tilde{R}_{SSS}$. In LTE, the PSS and SSS are closely located in time, enabling a potentially efficient coherent detection. In 5G NR, the PSS and SSS are not consecutive but are separated in time by one OFDM symbol, containing PBCH. Anyway, coherent detection could still be a viable solution, since the duration of the OFDM symbols can be 2^μ times shorter than LTE.

Our aim is to translate these concepts from LTE to 5G and compare these different approaches in order to determine the most efficient one.

In Table 4, we reported the complexity of the previously described detection techniques that are implemented and compared in the 5G simulator.

3.6 PBCH channel detection at the UE

The custom simulator already provided the functional blocks for the detection of DMRS and the decoding of the PBCH, compliant with the 3GPP standard, explained in the two following sections.

3.6.1 Detection of DMRS sequence for PBCH (SSB index determination)

There are 4 or 8 (depending on the frequency band) possible DMRS from where the actual DMRS of a certain SSB can be chosen. The receiver must then detect this particular DMRS by correlating the samples in the right positions with the locally known replicas. The detection permits to determine i_{SSB}, the LSB of the SSB index: 2 LSB (b_1, b_0) and half frame bit n_{hf} for $L_{MAX} = 4$, while 3 LSB (b_2, b_1, b_0) for $L_{max} = 8$ or $L_{max} = 64$.

Since the right DMRS should then be known at the receiver side, it can be exploited as a sequence of pilot symbols to estimate the channel. These estimates can be interpolated to compensate for the channel response in the PBCH symbols positions.

3.6.2 PBCH polar decoding

This procedure consists of stages similar but inverse to those performed by the transmitter:

Demodulation and demapping The SSB samples in the PBCH subcarrier positions (Table 2) can be collected and then QPSK demodulated, to pass from complex-valued modulation symbols to bits. Actually, the decoding of the block is more effective using

soft symbols, and then soft bits, instead of hard-demodulated bits. The simulator must compute the log-likelihood ratio (LLR) of each symbol and then move to the LLR of the single bits.

Descrambling (second scrambling) Since the LSB of the SSB index are given by the detected DMRS, the mask applied at the transmitter for the 2nd scrambling can be removed by generating and multiplying it with the received soft bits.

Rate dematching and polar decoding Only the first $N = 512$ bits are kept, since the last $E - N = 864 - -512 = 352$ bits are simply the repetition of the first ones. Note that this redundancy could be exploited by combining the repeated LLR. The soft bits are then passed to a polar decoder, a list successive cancellation (LSC) decoder CRC aided [36], with a list size of 8. This means that the outputs are the 8 codewords with the bigger likelihood, but only the one which carries a correct CRC is kept. Polar decoding then outputs a sequence of bits, hopefully corresponding to the transmitted info vector (hard decoding). The table containing the reliability sequence for the bits indexes in [25] can be used to determine the frozen bit positions, which are fixed for 5G NR polar codes.

CRC calculation and removal CRC is used by the LSC decoder and then removed.

Descrambling (first scrambling) The bits needed to mask the PBCH payload the first time are left unmasked, so they can used to generate the 1st scrambling sequence, to undo the first scrambling operation.

Deinterleaving The particular mapping applied at the transmitter side is known by the UE, so it can proceed with the demapping and finally recover the PBCH payload.

4 Results and discussion

In the previous sections, we described the main synchronization steps and different techniques that can be applied for 5G NR. The scope of this section is to present the most interesting results collected during many tests and simulations, from the simplest AWGN channel to more realistic scenarios. Ultimately, we provide results for real captures of 5G NR signals. An overview of the set of parameters for 5G NR systems can be found in [21], while the main system parameters adopted in our work are reported in Table 5.

We select a configuration with SSB bursts composed by eight SSBs, lying in the first half of the frame (i.e. during the first 5 ms). More precisely, these eight SSBs are transmitted during the first four slots of the frame, leading to two SSBs per slot, organized as in Fig. 1b: The first SSB occupies OFDM symbols from #2 to #5, and the second SSB occupies OFDM symbols from #8 to #11. As a simplification, the SSB is kept in the centre of the bandwidth, instead of adopting the synchronization raster as described by 5G NR specifications. This aspect can be neglected since it does not compromise the consistency of results.

4.1 AWGN channel

A very simple simulation scenario is the case of a single transmitting and receiving antenna, i.e. single-input single-output (SISO) configuration, and a simple channel model such as the AWGN channel. In this situation, we fix a reasonable SINR level, such as -6 dB, and we analyse the behaviour of the PSS detector with respect to different values of CFO. As shown in Fig. 5a, there are almost no missed detections up to a CFO of

Table 5 Main system parameters

Parameter	Value
Carrier frequency f_c	3.6 GHz
System configuration	SISO or 32×4 MIMO
Numerology μ	1
Subcarrier spacing $\Delta f_{SCS} = 15 \cdot 2^\mu$ kHz	30 kHz
Slot or transmission time interval TTI $= 1 \cdot 2^{-\mu}$ ms	0.5 ms
Signal bandwidth B	80 MHz
Sampling frequency f_s	122.8 MHz
FFT dimension per OFDM symbol N_{FFT}^{sys}	4096
SSB bandwidth	7.2 MHz
Downsampling factor	16
FFT dimension per OFDM symbol after downsampling N_{FFT}	256
SSB burst	8
SSB periodicity	20 ms
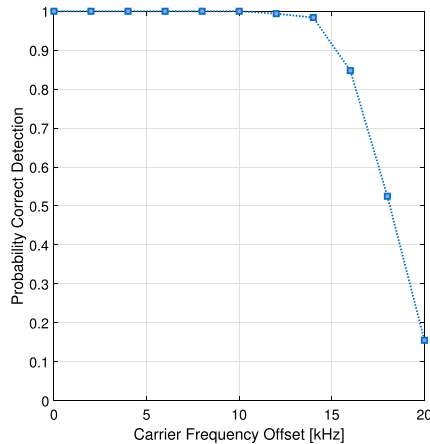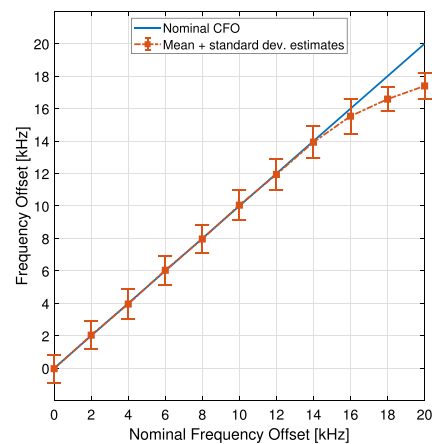
(a) Detection probability.   (b) CFO estimation.

Fig. 5 PSS detection at SNR of -6 dB for different CFOs

12 kHz, and then, the number of correctly detected sequences starts to decrease pretty rapidly. Using different values of IFO allows a better detection also for CFOs higher than 15 kHz (or lower than -15 kHz). In Fig. 5b, the mean and the standard deviation of the estimated CFO are reported. The estimation appears accurate but lacks precision. With a higher number of antennas and a longer detection period (up to 80 ms), the estimated values could be averaged both over space and time. A CFO refinement could be performed in further steps, but the need to refine it during the synchronization procedure should be evaluated by looking at the block error rate of PBCH, in order to avoid a complexity rise. For both the PSS and SSS detectors, the threshold for the peak comparison is tuned to keep the false positive probability not bigger than 10^{-2}.

Another interesting test is to identify which kinds of errors are given by the detector. Practically always the non-correctly detected PSSs correspond to the missed detection case, and very rarely (and only for extremely low levels of SINR) the detector chooses

Tuninato *et al. J Wireless Com Network*   (2023) 2023:111

Page 20 of 29
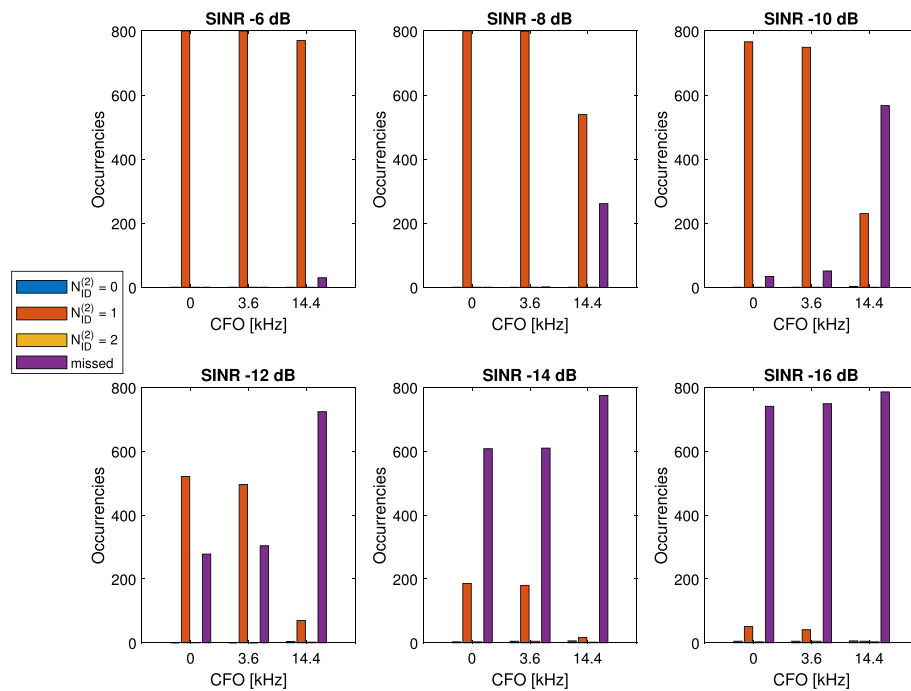
Fig. 6 PSS missed detection histograms, taking into account the possible kind of errors

the wrong $N_{\mathrm{ID}}^{(2)}$ (Fig. 6). This result proves the good cross-correlation properties of the adopted M-sequences in the time domain.

In the methodology section, three different techniques are presented to face SSS detection. We are interested in testing the robustness of the SSS detection with respect to a hypothetical RFO, in case the previous block failed to compensate the CFO correctly. Differently from PSS, when dealing with SSS, the CFO translates into ICI, which could severely harm the detection, and it is more difficult to correct than a frequency offset. In Fig. 7, the brute force, the FWHT, and the sequential techniques are compared, for different levels of RFO. With no RFO, missed detection results of the two former techniques outperform the latter, with loss in the order of 4 dB. In the case of an RFO of 7.2 kHz, the degradation of the missed detection is about 2 dB and up to 5 dB for 14.4 kHz. As we could have expected, SSS detection is less robust to frequency offset than PSS detection. Furthermore, we demonstrate that the sequential technique is not appealing from a performance point of view, and, since FWHT guarantees low complexity, we can remove this technique from the candidates of our system.

4.2 Fading channel

After the analysis of the main aspects of PSS and SSS in the simplified case of the AWGN channel, we move towards a more realistic and interesting system, with the use of a fading channel with a CDL-B profile and a MIMO configuration with 32 antennas at the transmitter and four antennas at the receiver (32×4 MIMO). The antennas at the transmitter are used for beam sweeping, with a set of beams covering the cell region taken from a DFT codebook [37, 38]. The tests considered the use of beamforming at the transmitter, but only the best beam is used, i.e. the one directed
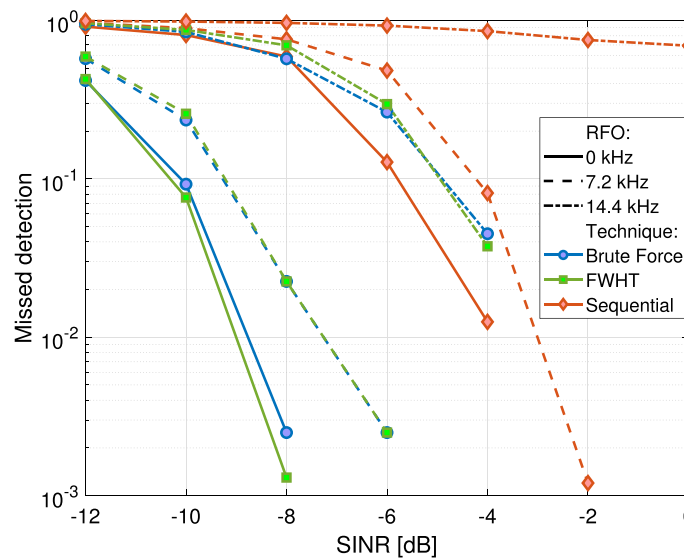
Fig. 7 SSS detection techniques comparison with different RFO, in AWGN channel

to the user, keeping it fixed for all the SSB transmissions, to reduce the time required for the simulations. However, each SSB within the SSB burst will still be considered independently, with the constraint of combining it, if necessary, only among the ones with the same beam index in subsequent bursts. At the receiver side, spatial diversity is exploited to improve the detection by non-coherently accumulating the correlation outputs, and averaging the CFO estimation among the four estimations. The CFO measure is further improved by accumulating the estimation in a window of up to 80 ms, i.e. four different SSB bursts.

Two different cases are then designed in order to test two different values of delay spread, namely "NOMINAL" and "LONG", definitions taken from 3GPP specifications.

Case 1: "NOMINAL" DS (100 ns) Setting this DS results in a coherence bandwidth of 10 MHz, bigger than the bandwidth occupied by the SSB. The PSS detection behaviour is shown in Fig. 8a, confirming the robustness against CFO and low SINRs. For what concerns SSS detection (Fig. 8b), as we already pointed out, the brute force and FWHT techniques return similar results. With this level of DS, the most simple version of the SSS detection, i.e. the non-coherent full block, is the one performing better than the other two. This is an important result since we could state that we can keep the simplest version of the decoder. In Fig. 10a, we can see the PBCH BLER behaviour, where the three PBCH curves for different CFOs are pretty similar (less than 1 dB loss), thanks to CFO compensation. This could let us avoid a finer CFO estimation in the previous blocks. These three curves are affected by the possible errors of the PCID detection. Comparing them with the ideal case (i.e. perfect knowledge of PCID), we can affirm that very small losses are introduced by PSS and SSS detection. Better results could be still obtained if the PBCH is soft combined through different SSBs.

Case 2: "LONG" DS (300 ns) In this second case, the coherence bandwidth is 3.3 MHz. We underline that this is quite an extreme DS for the chosen system
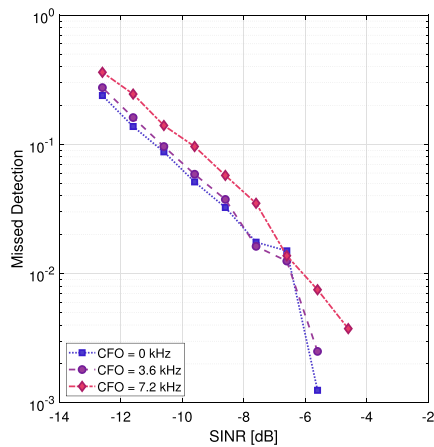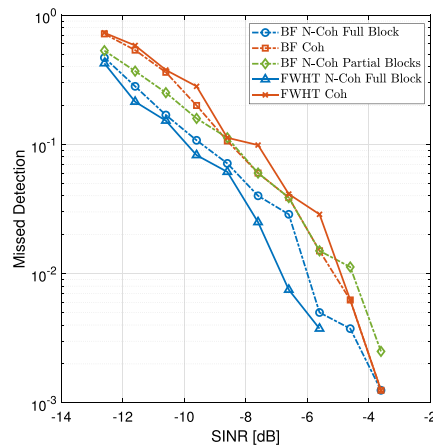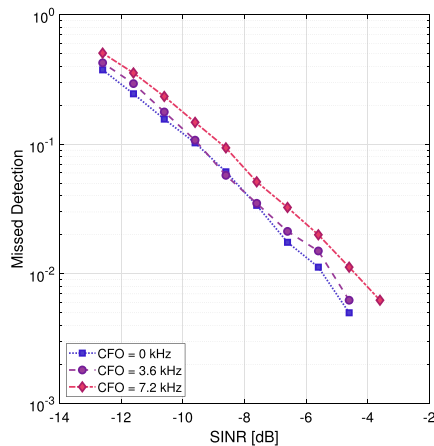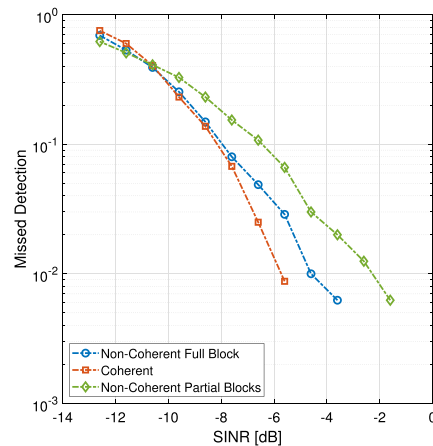
(a) PSS detection.   (b) SSS detection.

Fig. 8 Fading channel and "NOMINAL" DS

(a) PSS detection.   (b) SSS detection.

Fig. 9 Fading channel and "LONG" DS

parameters. The results for PSS are similar to before (Fig. 9a), except for a loss of up to 1 dB. The interesting point is to look at the differences between the SSS detector approaches, i.e. the coherent and non-coherent ones (Fig. 9b). As we could have expected, the coherent version permits to obtain lower missed detection for a certain range of SINR. Anyway, it does not appear as a huge improvement, and the extra complexity introduced by the compensation step should be weighted.

The harmful effect of CFO for PBCH decoding can be better visualized in Fig. 10b, where the detector is ignoring CFO compensation. The PBCH BLER is reported both in perfect detection, with PCID directly provided to the decoder, and actual PCID detection, with PSS and SSS. The curves for these two instances almost overlap, highlighting the CFO, and thus ICI, as the major impairment for PBCH decoding failure.

(a) "NOMINAL" DS

(b) No CFO compensation scenario.
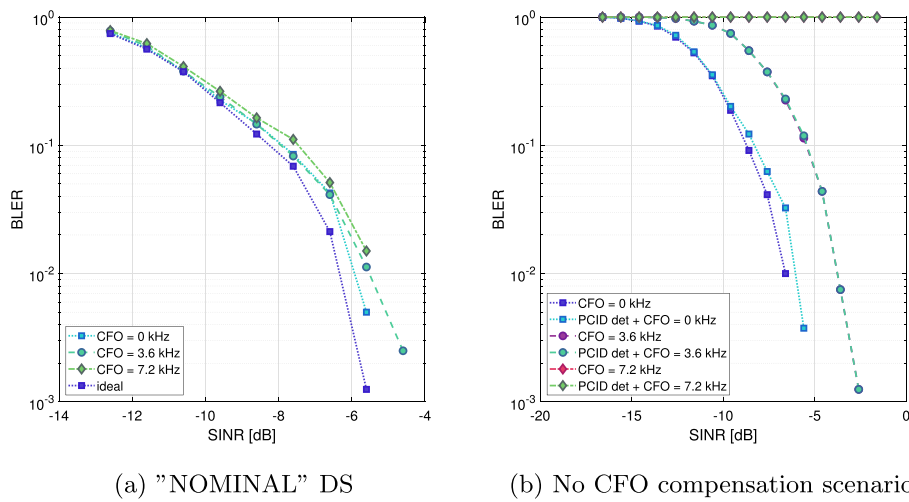
Fig. 10 PBCH decoding BLER for fading channel

4.3 PBCH comparison between LTE and 5G NR

In LTE, the PBCH encoding was performed through tail-biting convolutional coding with rate 1/3 and bit repetition by a factor 16 [39–43]. The choice of using polar codes for 5G NR is meant to improve the decoding capabilities at the receiver side, since this kind of code approaches (at least theoretically) the Shannon capacity.

In order to show the advance of the new specification, in Fig. 11, the BLER curves of 5G NR and LTE are reported. The system parameters are almost the same to guarantee fairness, and the fading channel is different than previous simulations: Extended Pedestrian A (EPA) channel with medium correlation, PBCH soft combination over 4 radio frames, and MIMO 2×2 and user speed of 2.16 km/h for LTE and 3 km/h for 5G NR. Actually, for 5G NR, the two transmitting antennas perform beamforming
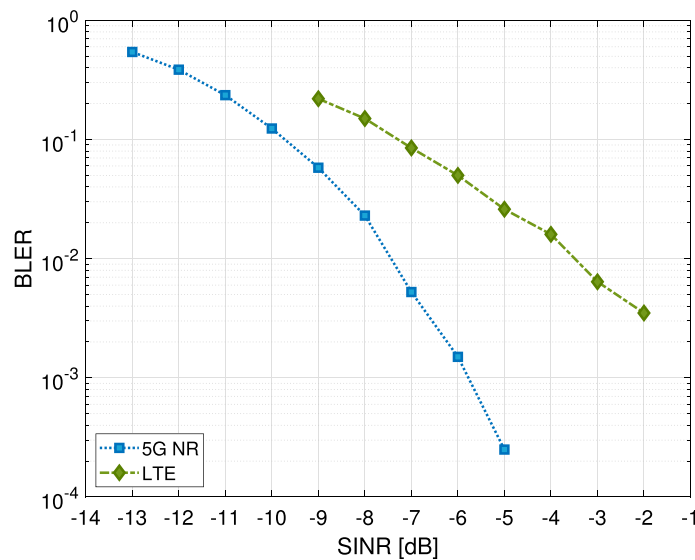
Fig. 11 PBCH decoding BLER: 5G NR vs LTE

(supposing perfect alignment with the receiver), while LTE relies on space–frequency block coded OFDM. It is not straightforward to compare the two systems, but we can still appreciate an improvement of about 1.5 dB of 5G NR, noticing also that 5G NR PBCH has a code rate more than $3\times$ higher: In LTE, the code rate is 1/48, while for 5G NR, it is 1/15.

4.4 Real captures

In order to prove the proper implementation of the receiver blocks, we used two captures of a real 5G NR signal, taken in an anechoic chamber. They are I/Q signals sampled at 7.68 Msample/s after a low-pass filter, which extracts the SSB from the wideband NR signal. The samples can be loaded into the MATLAB simulator and can be subjected to the previously described processing.

(a) Capture A.   (b) Capture B.
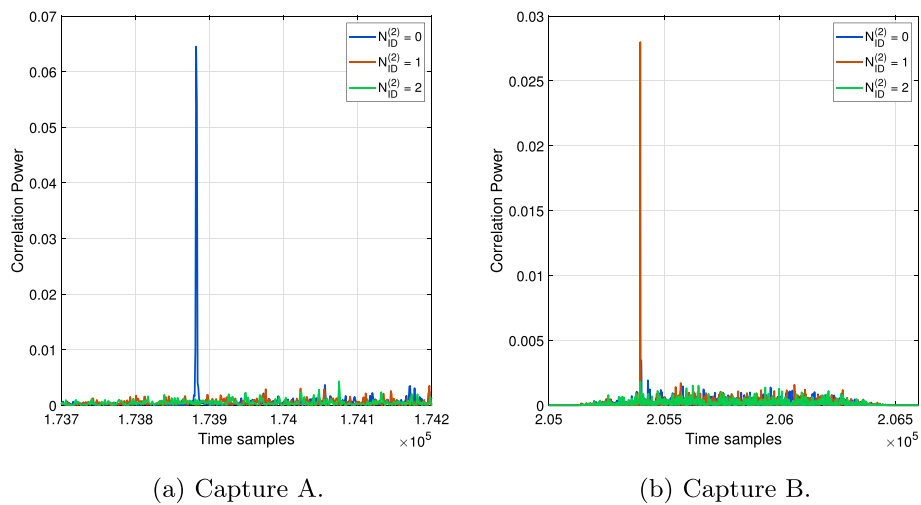
Fig. 12 Real 5G NR signal PSS detection, with focus on the main beam

(a) CFO effect on correlation.   (b) Beam-sweeping overview.

Fig. 13 Real 5G NR signal capture A

(a) SSS detection.
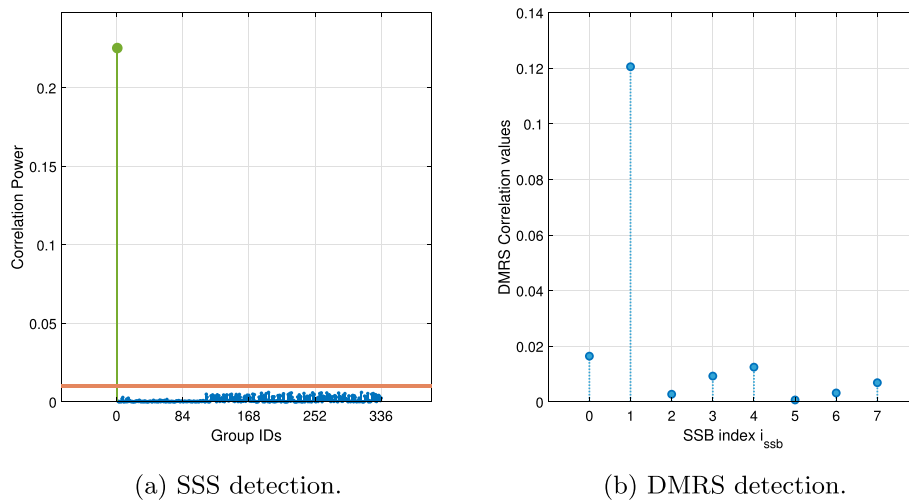
(b) DMRS detection.
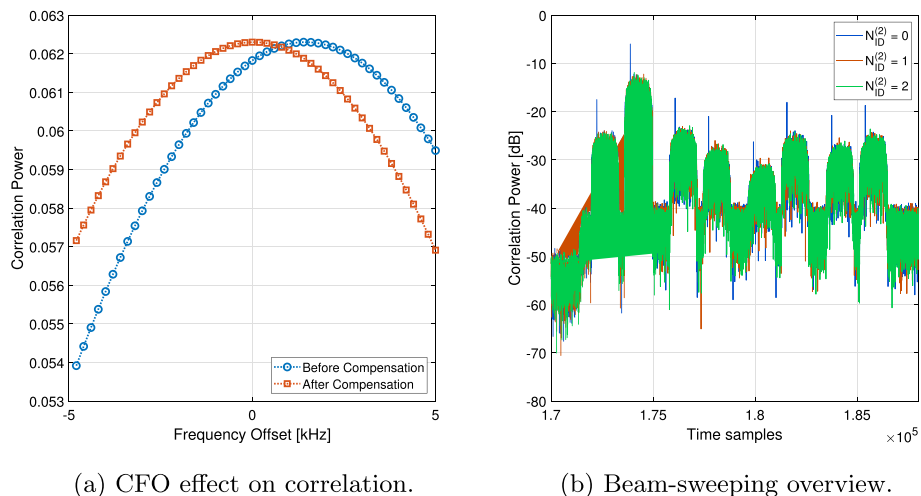
Fig. 14 Real 5G NR signal capture A

Capture A The transmitter is performing beam sweeping with eight beams, and one of them is received with a gain of at least 10 dB higher than the others. The beam sweeping result can be appreciated from the output of the PSS detector (Figs. 12a and 13b), where there is a very high peak of correlation for $N_{\mathrm{ID}}^{(2)} = 0$ related to the beam directed to the receiver, but there are also smaller peaks relative to PSSs inside the other beams. The CFO effect on the correlation peak is shown in Fig. 13a, which can be corrected with the CFO compensation. After the time alignment and the OFDM demodulation, the SSS detector can be used to find the $N_{\mathrm{ID}}^{(1)} = 0$ (Fig. 14a). Another interesting step is finding the correct DMRS sequence, the generation of which depends on the i_{SSB}, i.e. the index of the SSB with respect to the beam. In this case, the actual beam is the second one, corresponding to $i_{SSB} = 1$ (it starts from zero).

Capture B The transmitter is not performing beamforming, so only one SSB could be received. From the PSS detector (Fig. 12b), it is clear that no beam sweeping is performed, and only one SSB is transmitted each period. The other blocks return similar results as Capture A.

5 Conclusions

In this paper, we presented a comprehensive and detailed analysis of the 5G NR synchronization procedure, considering the entire sequence of functional blocks. The new definition of the SSB for 5G initial access aims to improve the probability of successful cell search by the users and to provide more flexibility in the resource management by the BS. Of particular interest is the robustness of the synchronization procedure in case of very low SINR and in difficult CFO conditions. We investigated many solutions, to compare their results with a realistic 3GPP-compliant channel model and to derive more insights on the implementation aspects. The choice of the 5G standard to adopt the M-sequences for PSS generation proved to be an effective solution to overcome the problem of the LTE Zadoff–Chu sequences and to improve the correlation

gain, but awareness must be taken on the downsampling step. We also provided some considerations on the domain of detection to better clarify the PSS properties. For what concerns SSS detection, we proved that the FWHT technique can guarantee excellent performance with a lower complexity than brute force detection. To overcome the effect of delay spread, different approaches were presented for LTE. We transferred those solutions to our 5G NR system, highlighting the potential of coherent detection in extreme delay spread conditions. Moreover, the use of polar codes for PBCH in 5G permits to outperform the previous LTE BLER results, but the CFO must be properly compensated in the previous stages. The simulator provided a MIMO configuration too, emulating the beam sweeping operation. To improve the CFO estimation, we exploited the accumulation along space (different antennas) and time resources, but other techniques could be considered in order to not increase the delay, for example exploiting the SSS. The blocks developed inside the simulator proved to be effective also for real captures of 5G NR signals, confirming the validity of the presented system. We are confident we provided a valuable benchmark and useful guidelines for current 5G, and further 6G, study and system deployments on initial access. In future, the synchronization procedure analysis could target cell-free mobile networks, a promising paradigm for the next generation of mobile networks. Moreover, new studies could target the use of machine learning techniques, such as reinforcement learning, to improve the synchronization technique by exploiting collected data by the base stations.

Abbreviations

LTE	Long-term evolution
NR	New Radio
BS	Base stations
UE	User equipment
OFDM	Orthogonal frequency-division multiplexing
SSB	Synchronization signal block
PCID	Physical cell identity
PSS	Primary synchronization signals
SSS	Secondary synchronization signals
PBCH	Physical broadcast channel
DMRS	Demodulation reference signals
SISO	Single-input single-output
MIMO	Multiple-input multiple-output
AWGN	Additive white Gaussian noise
DS	Delay spread
CFO	Carrier frequency offset
RFO	Residual frequency offset
ICI	Intercarrier interference
SINR	Signal-to-interference-plus-noise ratio
BLER	Block error rate
CP	Cyclic prefix
OTFS	Orthogonal time–frequency space
LFSR	Linear-feedback shift register
SFN	System frame number
TTI	Transmission time interval
MIB	Master information block
LSB	Last significant bits
MSB	Most significant bits
RMSI	Remaining minimum system information
NLOS	Non-line-of-sight
FFT	Fast Fourier transform
IFFT	Inverse fast Fourier transform
SCS	Subcarrier spacing
RB	Resource block

IFO   Integer frequency offset
FFO   Fractional frequency offset
FWHT   Fast Walsh–Hadamard transform
LLR   Log-likelihood ratio
LSC   List successive cancellation
CRC   Cyclic redundancy code
EPA   Extended pedestrian A
BPSK   Binary phase shift keying
QPSK   Quadrature phase shift keying
QAM   Quadrature amplitude modulation

Availability of data and materials
The datasets of the simulator results analysed during the current study are available from the corresponding author on reasonable request.

Declarations

Competing interests
The authors declare that they have no competing interests.

References
1. K. Ota, A. Shimura, M. Sawahashi, S. Nagata, Performance of physical cell ID detection probability considering frequency offset for NR radio interface. In: 2019 IEEE 90th Vehicular Technology Conference (VTC2019-Fall), pp. 1–6 (2019). https://doi.org/10.1109/VTCFall.2019.8891182
2. D. Wang, Z. Mei, H. Zhang, H. Li, A novel PSS timing synchronization algorithm for cell search in 5G NR system. IEEE Access **9**, 5870–5880 (2021). https://doi.org/10.1109/ACCESS.2020.3048692
3. F. Chen, X. Li, Y. Zhang, Y. Jiang, Design and implementation of initial cell search in 5G NR systems. China Commun. **17**(5), 38–49 (2020). https://doi.org/10.23919/JCC.2020.05.005
4. A. Omri, M. Shaqfeh, A. Ali, H. Alnuweiri, Synchronization procedure in 5G NR systems. IEEE Access **7**, 41286–41295 (2019). https://doi.org/10.1109/ACCESS.2019.2907970
5. M. Wang, D. Hu, L. He, J. Wu, Deep-learning-based initial access method for millimeter-Wave MIMO systems. IEEE Wirel. Commun. Lett. **11**(5), 1067–1071 (2022). https://doi.org/10.1109/LWC.2022.3156395
6. P. Wang, F. Berggren, Secondary Synchronization Signal in 5G New Radio. In: 2018 IEEE International Conference on Communications (ICC), pp. 1–6 (2018). https://doi.org/10.1109/ICC.2018.8422145
7. Y.-H. You, J.-H. Park, I.-Y. Ahn, Complexity effective sequential detection of Secondary Synchronization Signal for 5G New Radio communication systems. IEEE Syst. J. **15**(3), 3382–3390 (2021). https://doi.org/10.1109/JSYST.2020.3001925
8. J.-I. Kim, J.-S. Han, H.-J. Roh, H.-J. Choi, SSS detection method for initial cell search in 3GPP LTE FDD/TDD dual mode receiver. In: 2009 9th International Symposium on Communications and Information Technology, pp. 199–203 (2009). https://doi.org/10.1109/ISCIT.2009.5341260
9. V. Bioglio, C. Condo, I. Land, Design of polar codes in 5G New Radio. IEEE Commun. Surv. Tutor. **23**(1), 29–40 (2021). https://doi.org/10.1109/COMST.2020.2967127
10. Z. Jie, Z. Yun, S. Ling, Z. Ping, Effects of frequency-offset on the performance of OFDM systems. In: International Conference on Communication Technology Proceedings, 2003. ICCT 2003., vol. 2, pp. 1029–10322 (2003). https://doi.org/10.1109/ICCT.2003.1209705

11. Y.-A. Jung, S.-B. Byun, H.-J. Shin, D.-C. Han, S.-H. Cho, S.-H. Lee, Residual frequency offset estimation scheme for 5G NR system. In: 2021 Twelfth International Conference on Ubiquitous and Future Networks (ICUFN), pp. 273–275 (2021). https://doi.org/10.1109/ICUFN49451.2021.9528769

12. T. Strohmer, S. Beaver, Optimal OFDM design for time-frequency dispersive channels. IEEE Trans. Commun. **51**(7), 1111–1122 (2003). https://doi.org/10.1109/TCOMM.2003.814200

13. R. Hadani, S. Rakib, M. Tsatsanis, A. Monk, A.J. Goldsmith, A.F. Molisch, R. Calderbank, Orthogonal time frequency space modulation. In: 2017 IEEE Wireless Communications and Networking Conference (WCNC), pp. 1–6 (2017). https://doi.org/10.1109/WCNC.2017.7925924

14. P. Raviteja, E. Viterbo, Y. Hong, OTFS performance on static multipath channels. IEEE Wirel. Commun. Lett. **8**(3), 745–748 (2019). https://doi.org/10.1109/LWC.2018.2890643

15. M. Giordani, M. Zorzi, Non-terrestrial networks in the 6g era: challenges and opportunities. IEEE Netw. **35**(2), 244–251 (2021). https://doi.org/10.1109/MNET.011.2000493

16. Y. Zhang, H. Zhang, H. Zhou, K. Long, G.K. Karagiannidis, Resource allocation in terrestrial-satellite-based next generation multiple access networks with interference cooperation. IEEE J. Sel. Areas Commun. **40**(4), 1210–1221 (2022). https://doi.org/10.1109/JSAC.2022.3145810

17. M. Di Renzo, M. Debbah, D.-T. Phan-Huy, A. Zappone, M.-S. Alouini, C. Yuen, V. Sciancalepore, G. Alexandropoulos, J. Hoydis, H. Gacanin, J. Rosny, A. Bounceur, G. Lerosey, M. Fink, Smart radio environments empowered by reconfigurable ai meta-surfaces: an idea whose time has come. EURASIP J. Wirel. Commun. Netw.(2019) https://doi.org/10.1186/s13638-019-1438-9

18. H. Zhang, M. Huang, H. Zhou, X. Wang, N. Wang, K. Long, Capacity maximization in RIS-UAV networks: a DDQN-based trajectory and phase shift optimization approach. IEEE Trans. Wirel. Commun. **22**(4), 2583–2591 (2023). https://doi.org/10.1109/TWC.2022.3212830

19. 3GPP: Study on channel model for frequencies from 0.5 to 100 Ghz (release 16), ETSI TR 138 901 v16.1.0 (release 16). Technical report, 3GPP, Sophia Antipolis, France. Rep. TR **38**, 901 (2020)

20. D.G. Riviello, F. Di Stasio, R. Tuninato, Performance analysis of multi-user MIMO schemes under realistic 3GPP 3-D channel model for 5G mmWave cellular networks. Electronics **11**(3) (2022). https://doi.org/10.3390/electronics11030330

21. E. Dahlman, S. Parkvall, J. Sköld, 5g nr: the next generation wireless access technology, pp. 311–334. Academic Press, London (2018). https://doi.org/10.1016/B978-0-12-814323-0.00016-8

22. 3GPP: Physical channels and modulation (release 15) v15.2.0. Technical report, 3GPP, 3GPP, Sophia Antipolis, France. Rep. TS **38**, 211 (2018)

23. D. Chandramouli, R. Liebhart, J. Pirskanen, Radio Access Technology, pp. 51–126 (2019). https://doi.org/10.1002/9781119247111.ch3

24. 3GPP: 5G; NR; Radio Resource Control (RRC); protocol specification, ETSI TS 138 331 v15.3.0 (release 15). Technical report, 3GPP, Sophia Antipolis, France. Rep. TS **38**, 331 (2018)

25. 3GPP: 5G; NR; multiplexing and channel coding, ETSI TS 138 212 v15.2.0 (release 15). Technical report, 3GPP, Sophia Antipolis, France. Rep. TS **38**, 212 (2018)

26. Intel: NR PBCH design. Technical report, Intel Corporation (August 21th-25th, *3GPP TSG-RAN WG1 Meeting #90* (Czech Republic, Prague, 2017)

27. MediaTek: Way forward on PBCH bit mapping design. Technical report, MediaTek (28th Nov.–1st Dec. 2017). 3GPP TSG- RAN WG1 Meeting # 91 Reno, USA

28. E. Arikan, Channel polarization: a method for constructing capacity-achieving codes for symmetric binary-input memoryless channels. IEEE Trans. Inf. Theory **55**(7), 3051–3073 (2009). https://doi.org/10.1109/TIT.2009.2021379

29. Qualcomm: PBCH and PBCH DMRS design consideration. Technical report, Qualcomm (August 21th–25th, *3GPP TSG-RAN WG1 Meeting #90* (Czech Republic, Prague, 2017)

30. A. Goldsmith, *Wireless Communications* (Cambridge University Press, Cambridge, 2005)

31. D.G. Riviello, R. Tuninato, E. Zimaglia, R. Fantini, R. Garello, Implementation of deep-learning-based csi feedback reporting on 5g nr-compliant link-level simulator. Sensors **23**(2), 910 (2023). https://doi.org/10.3390/s23020910

32. E. Zimaglia, D.G. Riviello, R. Garello, R. Fantini, A novel deep learning approach to csi feedback reporting for nr 5g cellular systems. In: 2020 IEEE Microwave Theory and Techniques in Wireless Communications (MTTW), vol. 1, pp. 47–52 (2020). https://doi.org/10.1109/MTTW51045.2020.9245055

33. R. Tuninato, Algorithms for New Radio synchronization layer functions (CFO correction, PSS, SSS). Master Thesis, Politecnico di Torino, Department of Electronics and Telecommunications (2020)

34. 3GPP: User Equipment (UE) radio transmission and reception; part 1: Range 1 standalone (release 15) v15.2.0. Technical report, 3GPP (2018). 3GPP, Sophia Antipolis, France, Rep. TS 38.101-1

35. M. Cohn, A. Lempel, On fast M-sequence transforms (corresp.). IEEE Trans. Inf. Theory **23**(1), 135–137 (1977). https://doi.org/10.1109/TIT.1977.1055666

36. I. Tal, A. Vardy, List decoding of polar codes. In: 2011 IEEE International Symposium on Information Theory Proceedings, pp. 1–5 (2011). https://doi.org/10.1109/ISIT.2011.6033904

37. D.J. Love, R.W. Heath, Equal gain transmission in multiple-input multiple-output wireless systems. IEEE Trans. Commun. **51**(7), 1102–1110 (2003). https://doi.org/10.1109/TCOMM.2003.814195

38. 3GPP: Physical layer procedures for data; (release 16) v16.2.0. Technical report, 3GPP (2020). 3GPP, Sophia Antipolis, France, Rep. TS 38.214-1

39. H. Ma, J. Wolf, On tail biting convolutional codes. IEEE Trans. Commun. **34**(2), 104–111 (1986). https://doi.org/10.1109/TCOM.1986.1096498

40. 3GPP: LTE; Evolved Universal Terrestrial Radio Access (E-UTRA); physical channels and modulation; protocol specification, ETSI TS 136 211 v15.2.0 (release 15). Technical report, 3GPP, Sophia Antipolis, France. Rep. TS **36**, 211 (2018)

41. 3GPP: LTE; Evolved Universal Terrestrial Radio Access (E-UTRA); multiplexing and channel coding, ETSI TS 136 212 v15.2.1 (release 15). Technical report, 3GPP, Sophia Antipolis, France. Rep. TS **36**, 212 (2018)

42. 3GPP: LTE; Evolved Universal Terrestrial Radio Access (E-UTRA); physical layer procedures, ETSI TS 136 213 v14.2.0 (release 14). Technical report, 3GPP, Sophia Antipolis, France. Rep. TS **36**, 213 (2017)

Tuninato *et al. J Wireless Com Network*   (2023) 2023:111

Page 29 of 29

43. 3GPP: LTE; Evolved Universal Terrestrial Radio Access (E-UTRA); Radio Resource Control (RRC); protocol specification, ETSI TS 136 331 v15.3.0 (release 15). Technical report, 3GPP, Sophia Antipolis, France. Rep. TS **36**, 331 (2018)

Publisher's Note
Springer Nature remains neutral with regard to jurisdictional claims in published maps and institutional affiliations.